Accepted Manuscript

Mechanical performance of epoxy coated AR-glass fabric Textile Reinforced Mortar: Influence of coating thickness and formulation

Massimo Messori, Andrea Nobili, Cesare Signorini, Antonella Sola

Mechanical performance of epoxy coated AR-glass fabric Textile Reinforced Mortar: Influence of coating thickness and formulation

Massimo Messori[a], Andrea Nobili[a,*], Cesare Signorini[b], Antonella Sola[a]

[a]Dipartimento di Ingegneria Enzo Ferrari, via Vivarelli 10, 41125 Modena, Italy
[b]Dipartimento di Scienze e Metodi dell'Ingegneria, via Amendola 2, 42122 Reggio Emilia, Italy

Abstract

The mechanical performance of epoxy coated AR-glass fabric reinforced composite is investigated. A three-stage manufacturing process is considered, which involves fabric surface functionalization, liquid coating deposition and long-term setting and finally fabric embedment in the mortar matrix. Two epoxy coatings are considered, which differ only by the hardening agent. However, coating thickness is significantly diverse as a result of modified viscosity during liquid deposition. Performance is assessed in uni-axial tension as well as in three-point bending and it is expressed in terms of strength curves, data dispersion, crack pattern and failure mechanism. Remarkably, despite being very similar, the analyzed coatings produce a significantly different performance, especially when data dispersion is incorporated and design limits are considered. Indeed, although both coatings are able to consistently deliver fabric rupture at failure, only the thinnest is associated with small data scattering and an almost plastic post-peak behavior in bending. The associated design elongation limit reaches the maximum allowed value according to the ICC guidelines. In fact, it appears that coating thickness plays a crucial role in determining mechanical performance and fabric flexibility. The proposed manufacturing process proves extremely effective at enhancing matrix-to-fabric adhesion and thereby prevent

---

*Corresponding author

telescopic failure.

1. Introduction

Textile Reinforced Concrete (TRC) and Mortar (TRM), alongside the polymer-modified variation Fabric Reinforced Cementitious Material (FRCM), is gaining ground as a viable alternative to more traditional composite materials [4, 1, 3, 9], among which Fabric Reinforced Polymers (FRPs) stand out for their importance. Indeed, compared to these, TRC exhibits interesting advantages, which are deeply connected to the adoption of a cementitious-based matrix: in particular we mention durability, fire resistance, reversibility and ease of intervention, compatibility with traditional building materials and water vapour permeability [15, 12, 16]. On the other hand, in contrast to FRPs, interphase compatibility between the (cementitious) matrix and the fabric reinforcement is usually poor and this greatly hinders the full exploitation of the fiber mechanical strength [13]. This is especially true when multifilament yarns are employed, because interior strands (the so-called core zone) can hardly be reached by the matrix, whose low penetrability affords contact only with the outer strands (the sleeve zone). As a consequence, failure occurs in a distinctive "telescopic pullout" manner, i.e. through sliding of inner over outer strands (just as in the unfolding of a telescope) [6, 5].

To address this weakness, fibre-matrix interphase modification can be considered and polymer coating comes as a natural choice to capitalize on the experience with FRPs [11, 18]. Mineral coating agents may be considered instead, such as silica, carbon nanotubes (CNT) and nanoclays, especially when fire resistance is a serious concern [6, 14, 19]. Polymer-based liquid impregnation agents can be employed at the lamination stage (wet phase) and their action mechanism is clearly related to their capacity to bridge the fabric-to-matrix interface [16]. This bridging effect can be further improved adding fillers to the resin [7].

2

The desire to streamline production, increase reproducibility and reduce labour-cost suggests to consider industrial coating for the fabric. Epoxy coating is already proven to contribute to defect healing and fabric durability [10]. Remarkably, a small minority of studies is available in the literature assessing the role of epoxy coatings in improving mechanical performance of TRM, with special regard to coating formulation and thickness. Furthermore, existing studies consider out-of-the-box application of commercially available proprietary coatings, for which little data is accessible.

In [6], the role of organic and inorganic nanofillers on the mechanical performance of AR-glass TRC is investigated . Nanofillers act as an extra adhesion/frictional phase and they are applied to the glass bundles according to two different strategies: wet and dry. It is found that mechanical performance is strongly dependent on filler particle type and application strategy. In likewise manner, [8] investigates the effect of epoxy coated multifilament carbon fabric on the tensile, pull-out and fluid absorption capacity of TRC. Fabric is embedded in Portland cement and few details are available on the coating procedure. In [7], epoxy coating of carbon fabric in a cementitious matrix is investigated. Coating is performed by manual application with a brush or a spatula, which introduces large uncertainty on coating quality and thickness uniformity (see also [16] for a case study example of data scattering connected to poor impregnation quality).

In this paper, we assess the mechanical performance of AR-glass fabric reinforced mortar-based composite. Two epoxy micro coatings are considered for the reinforcing fabric, which differ only by the hardening agent. A preliminary treatment is first considered to promote coating anchoring to the fabric surface (functionalization). Coating is applied by liquid deposition. Thus, uniform coating thickness is attained on the yarn, although liquid tends to lump on the fabric stitches. Coating thickness stands in the range of $300\,\mu$m depending on the specific epoxy formulation and plays a relevant role in affecting the overall performance. Besides, coating thickness has a strong bearing on fabric flexibility for it affects its capacity to closely follow irregular surfaces.

3

Characteristic	Unit	Value
Yarn count	tex	1200
Ultimate strength of the dry fibres	MPa	1400
Specific weight per unit fabric area	g/m^2	300
Fabric specific weight	g/cm^3	2.50
Grid spacing (square grid side)	mm	12
Glass fabric cross-sectional area (per unit width), A_f	mm^2/cm	0.60
Ultimate strength along the principal direction (epoxy impregnated)	MPa	1200
Elastic modulus	GPa	74

Table 1: ARG fabric mechanical properties (1 tex = 9 den)

2. Materials and methods

2.1. Fabric reinforcement

A bi-directional commercially available alkali-resistant (AR) multifilament fabric (Zirconglass Wire RV320-AR, Betontex) is used as reinforcement fabric (see Tab.1). A open square mesh grid is adopted.

2.1.1. Silanization

Glass fabric is preliminary treated to enhance chemical bond formation with the organic coating (functionalization). To this aim, 3-Aminopropyltriethoxysilane ($C_9H_{23}NO_3Si$, hereafter "silane") is chosen as coupling agent. The coupling agent is diluted with distilled water until a 2% vol. solution is obtained, that is stirred for 15 mins at room temperature. Glass fabric is immersed in this solution for 40 s, carefully rinsed with distilled water and then left to dry at room temperature. Distilled water has been preferred to organic solvents, such as ethanol or acetone, to preserve the integrity of the stitches connecting warp/waft yarns in the fabric mesh.

2.1.2. Epoxy coatings

Once functionalized, the ARG fabric is coated with epoxy resin. To this aim, high-purity bisphenol A diglycidylether resin ($C_{21}H_{24}O_4$, D.E.R. 332, DOW Chemicals, hereafter "DER") is reacted with two different curing agents: either the aromatic hardener m-phenylenediamine (hereafter "m-PDA"), also
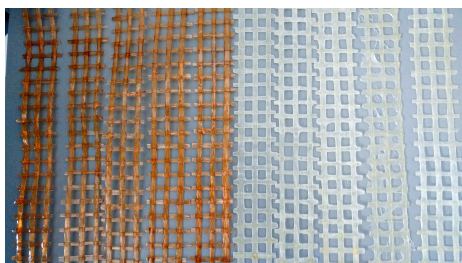
4

Figure 1: Coated ARG fabric after cross-linking: G-ER (left) and G-EW (right)

called 1,3-diaminobenzene ($C_6H_4(NH_2)_2$), or the organic aliphatic hardener diethylenetriamine ($HN(CH_2CH_2NH_2)_2$, hereafter "DETA"), also known as 2,2-Iminodi(ethylamine). DER is pre-heated at 50°C in a magnetic stirrer and mixed, in stoichiometric ratio, with m-PDA flakes or liquid DETA until complete homogenization. Glass fabric is bathed in either solution for 10 s, extracted and squeezed out to remove the excess of resin and then left to crosslink at room temperature. Accordingly, the following sample groups are investigated:

- uncoated ARG fabric (coded G-UC);

- silane functionalized ARG fabric coated with epoxy resin and m-PDA as hardening agent (G-ER);

- silane functionalized ARG fabric coated with epoxy resin and DETA as hardening agent (G-EW).

The two families of coated fabric are shown in Fig.1.

2.2. Inorganic matrix

A pre-mixed natural hydraulic lime (NHL) mortar, aimed at structural purposes (GeoCalce Fino®, Kerakoll SpA), is employed for all specimens. Its main properties are gathered in Tab.2. This fine aggregate matrix, endowed with superior ductility compared to Portland cement and good workability, promotes specimen reproducibility and diffuse cracking at failure [15].

5

Characteristic	Unit	Value
Mineralogy of the aggregates	-	siliceous/carbonate
Granulometry	mm	0 - 1.4
Nominal setting water content	%	21.2
Final density	g/cm^3	1.58
Compressive strength (28 days)	MPa	15
Flexural strength (28 days)	MPa	5
Shear adhesion on brick support	MPa	1
Elastic compressive modulus	GPa	9

Table 2: Mechanical and physical properties of the mortar matrix

2.3. Specimen preparation
2.3.1. Uni-axial tensile test

A minimum of five 1-ply ARG-TRM specimens (coupons) for each test group have been manufactured according to the ICC Guidelines [2]. As detailed in [15], specimen manufacture is carried out on an individual basis, to avoid cutting from a larger sheet, in a polyethylene formwork specially designed to warrant thickness uniformity of the matrix layers and consistent placing of the fabric at midplane. Coupon geometry is illustrated in Fig.2(a). The specimen width, w_f, is chosen to accommodate three fabric yarns and, consequently, it is an integer multiple of the grid spacing, i.e. $w_f = 36$ mm. Accordingly, fabric cross-section is $A_f = 2.16$ mm^2 . The modular formwork adopts 3-mm-thick pinned laths as specimen spacers and it is lubricated to ease stripping.

Manufacturing occurs as follows. The first layer of mortar is cast on the formwork and levelled up with the lath top surface with a scraper. The cut-to-size reinforcing fabric is placed and slightly pressed on the fresh mortar. A second layer of laths is placed on top of the first to provide guidance for fabric placing. Then, a second and final layer of mortar is applied on top up to the new lath level. As suggested in [2], to minimize warping due to differential water evaporation at the top/bottom specimen faces, 7-day moist curing is undergone in a tight polypropylene bag before stripping. Besides, given that curing time is found to play a very significant role on mechanical properties [17], extended 56-day curing is considered for all specimens. Finally, 100-mm-long glass fabric tabs are glued to the specimen ends through epoxy resin to provide a smooth
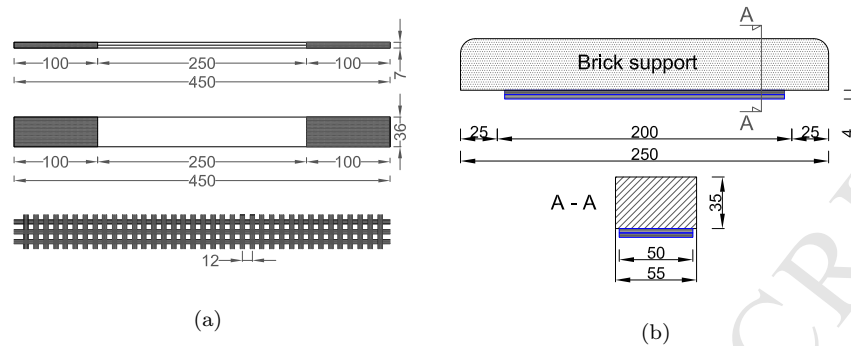
Figure 2: Specimen geometry (dimensions in mm): (a) rectangular coupons for uni-axial traction test and (b) three-point bending of laminated bricks

gripping surface for the clamps.

2.3.2. Flexural test

Laminated clay brick supports have been tested in three-point bending (3-PB), as illustrated in Fig.2(b). Although no provision against end delamination is taken, the design anchoring length $L_a = 100$ mm warrants that failure initiates at midspan, in the composite, and delamination only occurs eventually [16].

Specimen manufacturing takes place as follows.

- The support is preliminary polished and wetted to reduce surface tension; a pair of constraining laths are adopted to warrant a net resistant cross-section (see Fig.3(a));

- a thin layer of mortar is applied onto the support in between the constraining laths which provide a reference for the mortar level;

- fabric is placed on top and slightly pressed;

- formwork is extended and a second layer of mortar is placed and levelled.

The supporting brick exhibits a mean flexural strength of 4.3 MPa and the overall thickness of the composite is 4 mm. Specimens are 7-day moist cured, stripped and finally cured at laboratory conditions for 56 days in total (Fig.3(b)).
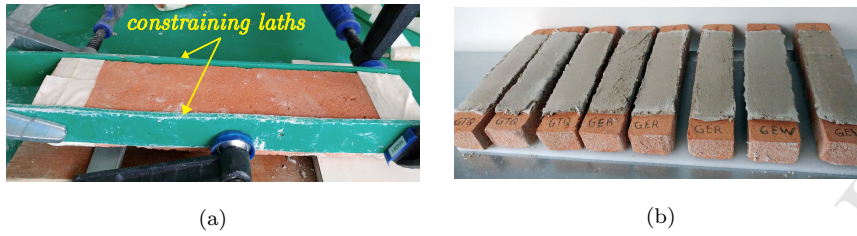
7

Figure 3: Three-point bending test specimen manufacture: (a) brick support with constraining laths (b) laminated specimens

3. Experimental investigation

The experimental campaign consists of mechanical tests and microscopy investigation aimed at assessing the quality of interphase bond formation.

3.1. Tensile tests

Uni-axial tensile tests are performed using a universal testing machine (UTM) Instron 5567, equipped with a 30 kN load cell and pneumatic wedge clamps. The top clamp is connected to the crosshead through a spherical hinge. The test is conducted under displacement control with fixed nominal displacement rate $\dot{\delta} = 0.5$ mm/min (as in [8]). This displacement rate, weighted against the specimen nominal gauge length $L_g = 250$ mm, complies with the prescription in [1] concerning the imposed strain rate $\dot{\varepsilon} = 2$ mstrain/min (compare with $\dot{\varepsilon} = 3$ mstrain/min in [7]). As already observed in [15], the displacement rate is really nominal for it is affected by the wedge extension during testing. Thereby, for better accuracy, the actual elongation rate is measured through a stereoscopic 3 Mpixel Dantec Dynamics Q-400 Digital Imaging Correlation (DIC) system operated with a sampling rate of 2 Hz. Measured data are line-fitted and the line slope is taken as the actual displacement rate, as shown in Fig.4.

3.2. Three-point bending test

Three-point bending tests are carried out using the same UTM equipped with a knife acting at midspan of a twin point-support clamp. Support spacing is set at 200 mm. Flexural test takes place under displacement control of the acting knife with a displacement rate $\dot{\delta} = 1$ mm/min.
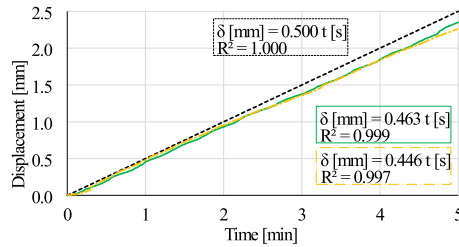
8

Figure 4: Uni-axial test nominal elongation ramp imposed at the UTM crosshead (dotted line, black) and actual elongation rate, as measured by DIC, for G-ER (solid, green) and G-EW (dash-dotted, yellow) specimen groups. Linear fitting expressions are also given alongside the coefficient of determination R^2

3.3. ESEM microscopy investigation

To analyze both epoxy-coated fabrics and failed specimens, the environmental scanning electron microscopy ESEM Quanta-200 is operated without metal coating in low vacuum (pressure $90.64\,\mathrm{Pa}$).

4. Results and discussion

4.1. Coating thickness

The average thickness (i.e. equivalent diameter) of the ARG fabric is shown in Fig.5 for the uncoated and coated groups. Thickness measures are taken at several different positions both on the yarns and on the stitches, where the coating solution tends to lump. The mean thickness of the reinforcement fabric sits below $300\,\mu$m for the yarn and it is almost twice as large at the stitches. The mean thickness of the epoxy coating is $t_{ER} = 338\,\mu$m in the G-ER group and $t_{EW} = 279\,\mu$m in the G-EW group, with standard deviation $\sigma(t_{ER}) = 17\,\mu$m and $\sigma(t_{EW}) = 1\,\mu$m, respectively. For interphase modification, mesh flexibility and response homogeneity, coating thickness should be as small as possible, while higher thickness proves beneficial for durability and defect-healing purposes. Although G-ER coating is only 21% thicker than G-EW, the corresponding specimens can be easily told apart in light of their greater stiffness.
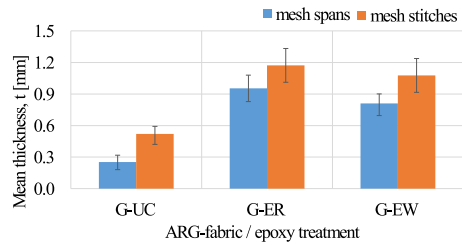
9

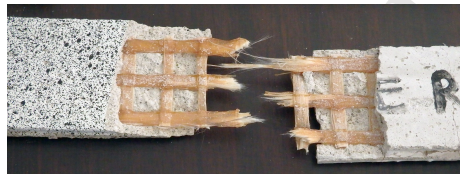Figure 5: Mean fabric thickness at the yarns and at the stitches

Figure 6: Fabric rupture is the typical failure mode in the G-ER and G-EW groups

Figure 7: Typical telescopic failure mode for brick bending in the G-UC specimen group

Figure 8: Typical delamination failure mode for brick bending in the G-ER and G-EW groups

4.2. Failure analysis

Fig.6 shows the typical failure mode taking place in the G-ER and G-EW groups and involving fabric rupture. In contrast, G-UC specimen failure always occurs in telescopic fashion and indeed the same mechanism is encountered in bending (Fig.7). Bending test of coated specimens ends by delamination failure, that is an expected consequence of the lack of shear strengthening provisions (Fig.8). However, strength curves clearly show the positive effect of coating on the mechanical response prior to failure (see Sec.4.6).

4.3. ESEM investigation of failed specimens

Figs.9 and 10 show ESEM magnification of the matrix-to-fabric interface of failed specimens. In particular, it appears that telescopic failure wipes the matrix off the multifilament yarns whenever the chemical bond is weak enough, as it is the case for G-UC specimens, see Fig.9(a). In contrast, both epoxy coatings provide enough substrate adhesion for the matrix to resist failure, as in Figs.9(b) and (c). Furthermore, in Fig.9(a) multifilaments stand well separated and identifiable in the yarn, while Figs.9(b-c) reveal only a few external filaments emerging from the epoxy coating. Indeed, at higher magnification, the latter appears as a solid block embedding the multifilaments. In Fig.10(a), small matrix particles occasionally stain the surface of full-round individual multifilaments, whereas in Fig.10(b) coated specimen strands appear embedded in solid resin. Moreover, it is clear that large and widespread patches of mortar are still well bonded to the solid resin, in contrast to multifilaments that support very few.

4.4. Uni-axial tensile test

Stress-strain curves obtained from uni-axial tension tests are gathered in Fig.11, where the same scaling is adopted for the axes to better appreciate performance comparison. As customary, strain is conventionally reported to the fabric cross-sectional area A_f. Looking at these curves, it is immediately clear that coated specimens exhibit remarkable ductility and strength gains over the uncoated group and, in this respect, the G-EW group performs best.
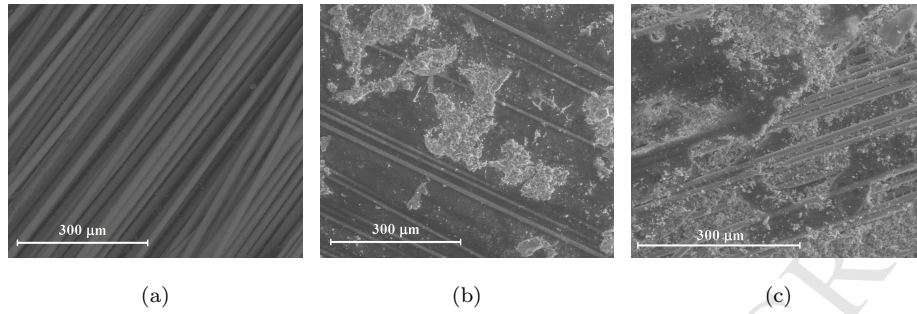
11

(a)   (b)   (c)

Figure 9: ESEM micrography at 400X magnification of G-UC (a) G-ER (b) and G-EW (c) failed specimens
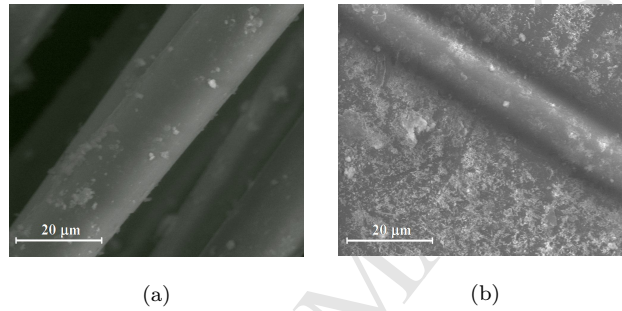

(a)   (b)

Figure 10: ESEM micrography at 4000X magnification of G-UC (a) and G-ER (b) failed specimens.

(a)   (b)

(c)

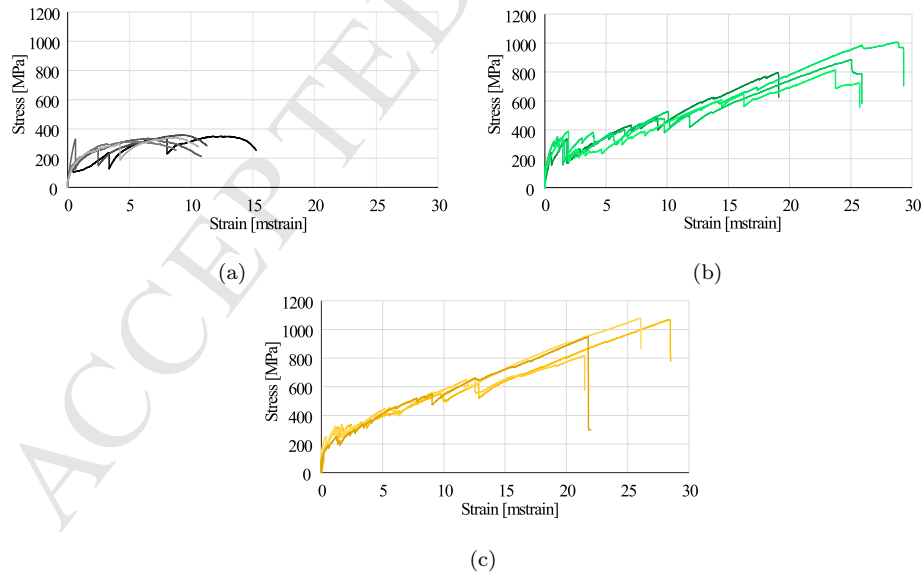Figure 11: Stress-strain curves for uni-axial traction of all tested specimens in the G-UC (a) G-ER (b) and G-EW (c) groups
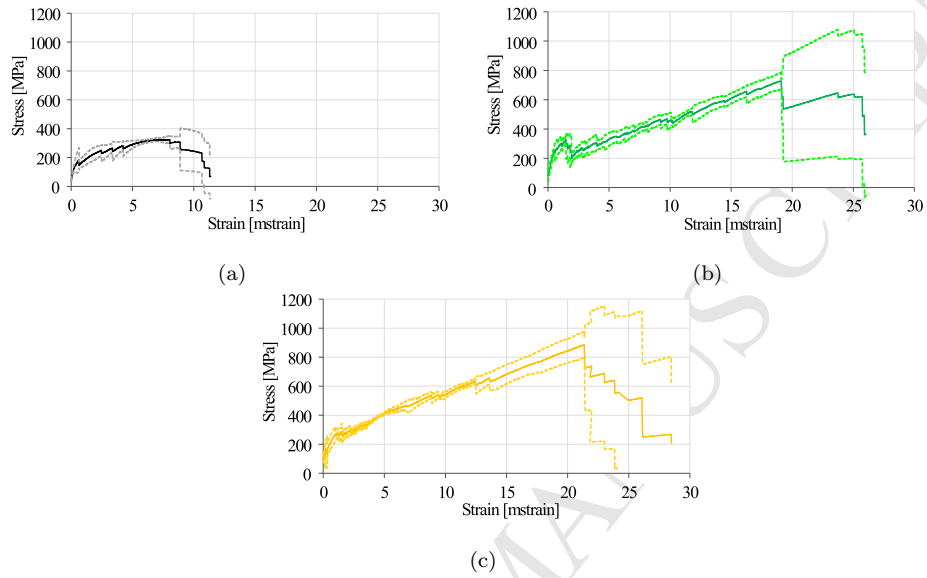
12

Figure 12: Mean stress-strain curve with ±1 standard deviation band for uni-axial traction of (a) G-UC, (b) G-ER and (c) G-EW specimen groups
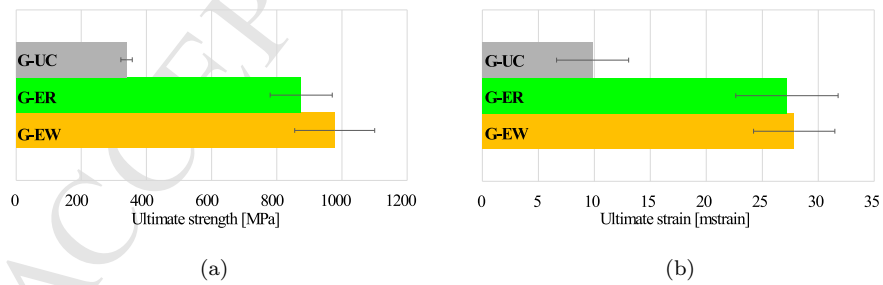

Figure 13: Mean ultimate stress (a) and mean ultimate strain (b) evaluated in uni-axial traction for all specimen groups

13

Group	Tensile strength			Tensile elongation		
	$\mu(f_{fu})$	σ_f	CV_f	$\mu(\varepsilon_{fu})$	σ_ε	CV_ε
	[MPa]		[%]	[mstrain]		[%]
G-UC	339	17	5.1	9.8	3.2	32.7
G-ER	875	95	10.9	27.2	4.6	16.8
G-EW	978	123	12.6	27.9	3.6	13.0

Table 3: Mean ultimate tensile strength $\mu(f_{fu})$ and elongation $\mu(\varepsilon_{fu})$, with corresponding standard deviation σ and coefficient of variation CV, for all specimen groups, as derived by uni-axial tension tests

Fig.12 plots the mean strength curve for each specimen group alongside the corresponding one-standard-deviation band. Comparing this picture with Fig.6 in [8], obtained for carbon fabric in Portland cement, we see similar ductility levels (ultimate strength at about $\varepsilon = 20$ mstrain) and yet remarkably superior mean performance increments over the uncoated fabric. A bar chart comparison of ultimate strength and strain values is presented in Fig.13.

Tab.3 collects the mean ultimate strength and strain values, together with the corresponding standard deviation σ and coefficient of variation CV, for all specimen groups. It appears that G-ER and G-EW coated specimens present a 158% and 188% increment in the mean ultimate strength $\mu(f_{fu})$ over the uncoated group G-UC, respectively. However, as expected, this remarkable strength gain comes at a significant cost in terms of data scattering, which is due to the well-known positive covariance effect [17]. To better assess the actual performance gain, design values should be compared instead. According to the minimum acceptable design criteria proposed in [2], a 3-sigma rule is adopted to evaluate the ultimate strain ε_{fu} and the ultimate design strain ε_{fd} therefrom

$$\varepsilon_{fu} = \mu(\varepsilon_{fu}) - 3\sigma_\varepsilon, \quad \varepsilon_{fd} = 0.7\varepsilon_{fu} \leq 1.2\%.$$

The design strength (at failure) may be evaluated from the design strain by multiplication by the crack longitudinal modulus E_f

$$f_{fd} = 0.85 E_f \varepsilon_{fd}, \tag{1}$$

or from experimental data, which is largely more realistic [17].

14

Group	Strength				Elongation	
	f_{fd} [MPa]	Δ [%]	f_{fuk} [MPa]	Δ [%]	ε_{fu} [mstrain]	ε_{fd} [mstrain]
G-UC	288	-	311	-	0.2	0.14
G-ER	590	105	719	131	13.4	9.4
G-EW	609	111	776	150	17.1	12.0

Table 4: Design tensile strength, f_{fd}, characteristic ultimate strength, f_{fuk}, ultimate elongation ε_{fu} and design elongation ε_{fd} for all specimen groups, as derived from uni-axial tension tests. Δ expresses the coated/uncoated ratio for the relevant characteristic.

Tab.4 presents design values for strength and elongation as determined from the experimental results through a 3-sigma rule, together with the ultimate characteristic strength f_{fuk} (this is obtained from the 1.64-sigma rule and it is really the characteristic value provided that a Gaussian distribution for the data is assumed). Data analysis supports some of the conclusions already discussed in [17] and it confirms that the 3-sigma rule is very conservative for it produces a very unfavourable design strain in the presence of the data scattering characteristic of brittle matrix composite materials. As a consequence, evaluation of the design strength from the design strain according to Eq.(1) produces a strong under-estimation of the experimental evidence. Indeed, in the uncoated group, design strain is drastically reduced by the comparatively large data scattering associated with telescopic failure. When experimental data are employed instead, the design and the characteristic strength associated with either coated group exceeds a two-fold increase over the uncoated group, almost independently of the coating type. In this respect, G-ER and G-EW appear almost equivalent and this conclusion seems to support the common action mechanism associated with epoxy coating, whose role is to prevent telescopic failure. However, results change significantly when elongation is considered. Although the mean ultimate elongation associated with the G-ER and G-EW groups is almost identical, i.e. $\mu(\varepsilon_{fu}) \approx 27$ mstrain, the standard deviation σ_ε is 22% smaller for G-EW compared to G-ER. This reduction in data scattering translates into a 28% improvement of the ultimate and design elongation. It is remarkable that data scattering in the G-EW group is close to that connected with the uncoated
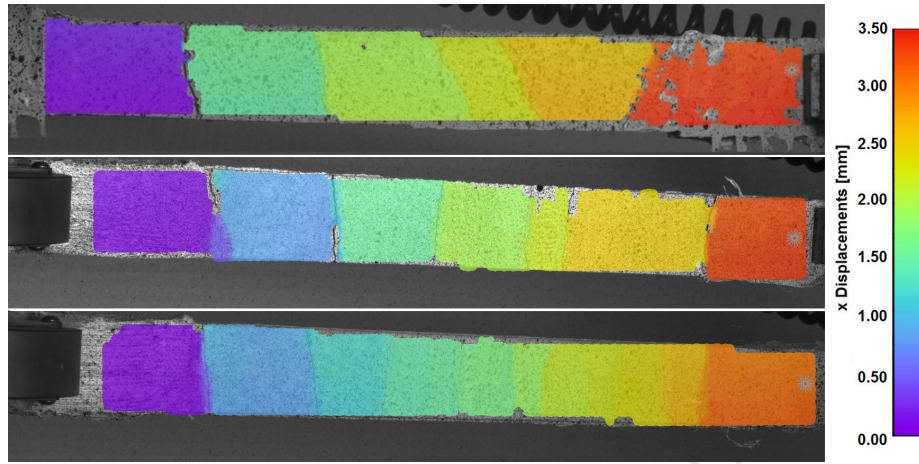
15

Figure 14: Longitudinal displacement field for ARG coupons at $\varepsilon = 15$ mstrain (from top to bottom: G-UC, G-ER and G-EW specimens)
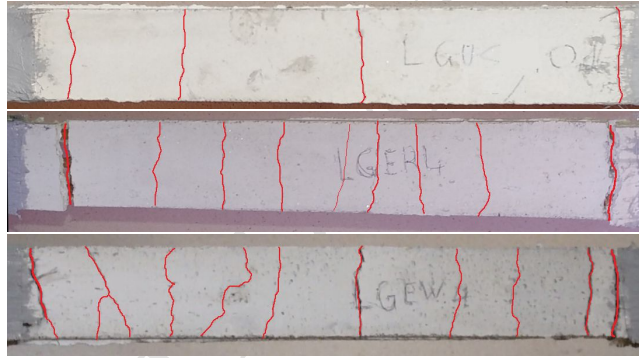

Figure 15: Near failure crack pattern in G-UC (top), G-ER (middle) and G-EW (bottom) specimens

group G-UC and yet the design elongation is 85-times greater. Furthermore, the design elongation of the G-EW group reaches the allowable maximum value 1.2% and, in this respect, it is an optimum value.

4.5. Crack pattern analysis

Determination of the crack pattern brings a significant contribution to the assessment of the energy dissipation capability associated with the failure mechanism [20]. Fig.14 shows a colour map representation of the axial displacement field for the three specimen groups at a common elongation value $\varepsilon = 15$ mstrain.
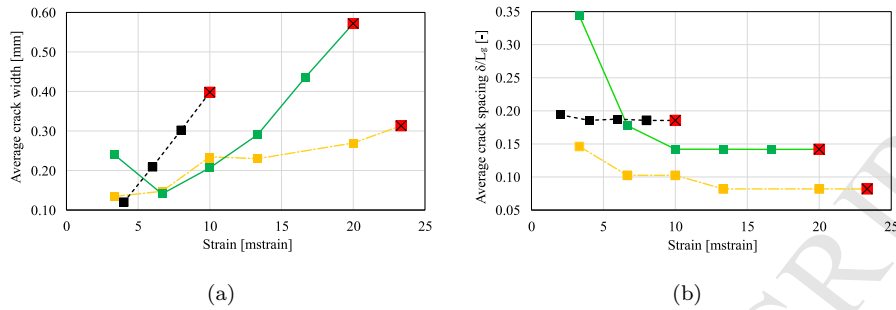
Figure 16: Mean crack width (a) and dimensionless crack mean spacing (b) vs. strain for G-UC (dotted, black), G-ER (solid, green) and G-EW (dash-dotted, orange)

As expected, specimen displacement mainly occurs in a discrete fashion, through crack widening, and the number of cracks is a good indication of the specimen ductility and energy dissipation capability. In this respect, the G-UC specimen features fewer cracks with larger displacement jumps compared to coated specimens. Fig.15 compares the near-failure crack pattern for G-ER and G-EW specimens, with the latter exhibiting better damage distribution and diffusion.

Estimation of the number of cracks and of the crack width is obtained from DIC data at different elongation values in uni-axial test. Figs.16(a) and (b) plot the average crack width and the crack average spacing as a function of the strain up to failure, respectively. The crack average spacing is normalized to the gauge length $L_g = 250$ mm. The failure point is denoted by a red square marker at the end of each curve. Curves support the qualitative conclusion that, at the same strain level, the uncoated specimen exhibits fewer cracks located at larger distance and those cracks are wider than those in the coated groups, with the partial exception of very low strain levels for which cracking is mainly induced by curing. Fig.16(a) shows that crack width increases with strain in an almost linear fashion with similar slope for all specimens (cf.[17]). However, the G-EW specimen closely follows the G-ER specimen until $\varepsilon = 10$ mstrain, that is the failure strain for the uncoated specimen, beyond which point it acquires a far smaller slope. Thus, it appears that the G-EW specimen features a strongly enhanced crack pattern diffusion, with several thin cracks located
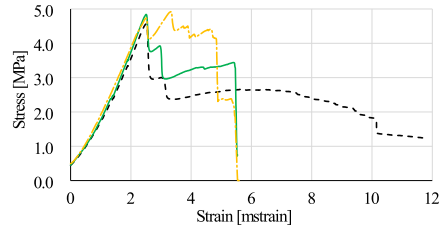
17

Figure 17: Mean stress-strain curves for three-point bending of clay bricks laminated with G-UC (dotted, black), G-ER (solid, green) and G-EW (dash-dotted, yellow) composite

at short distance, which seems to be the result of an apparently stiffer fabric, i.e. fabric telescopic slippage lowers the apparent elastic modulus. Indeed, Fig.16(b) shows that the crack average spacing for G-EW is about half as much as that for the uncoated specimen, the G-ER specimen faring in between. Crack spacing quickly plateaus for all groups and, in fact, the corresponding limit can be considered as a good indication of the coating effectiveness [17]. It is worth observing that, in contrast to the uncoated specimen for which crack average spacing is almost flat throughout, coated specimens exhibit decreasing curves, the decrease rate being most pronounced at small strain. It can be deduced that in coated specimens new cracks are able to open, especially at low strain levels, whereas in the uncoated specimen the number of cracks rest the same and the sliding mechanism of the embedded fabric brings the sole contribution to deformation through crack widening.

4.6. Three-point bending test

The strength curves of laminated clay bricks in three-point bending are presented in Fig.17. Stress is conventionally reported to the resistant cross-section

$$\sigma_{zz} = \frac{M_{xx}}{W_x},$$

where $W_x = 50 \times 35^2/6$ mm^3 is the resistance modulus. The stress peak is consistently reached at brick failure and it is the same regardless of the lamination type. Nonetheless, the post-peak behavior is strongly affected by the composite capacity to resist telescopic slippage and delamination. In this respect, it is clearly seen that G-EW specimens present an almost constant post-

18

peak strength (plastic behaviour), whereas G-ER perform in between uncoated and G-EW (softening behaviour). Since support adhesion is independent on the coating and no provision was taken against delamination, a superior performance in terms of strength inevitably leads to anticipated delamination, i.e. less ductility. Indeed, failure strain in the G-ER and in the G-EW group is virtually identical ($\varepsilon = 5.4$ mstrain) and it is located about halfway to the failure strain of G-UC.

5. Conclusions

The mechanical performance of epoxy coated AR-glass fabric composite has been considered. Preliminary functionalization of the fabric surface is adopted to enhance chemical bond formation with the coating. Two epoxy coatings are employed in a mortar matrix, which only differ in terms of hardening agent. Mechanical performance is assessed in uni-axial traction of rectangular specimens (coupons) and in three-point bending of laminated clay bricks. Failure mode analysis, crack pattern development and microscopy investigation are presented. As expected, coated specimens largely over-perform uncoated ones, for telescopic failure is averted and fabric rupture is reached. Somewhat surprisingly, a relatively small difference in the coating thickness (G-EW coating is 17% thinner than G-ER owing to reduced viscosity in the liquid phase) produces a strong effect in the final performance. Indeed, although mechanical performance appears very similar when mean failure strength is considered, and in fact almost identical in terms of mean elongation at failure, coating thickness has a strong bearing on data scattering and results take on a different perspective when looked under the viewpoint of design limits. This conclusion is indeed supported by failure analysis, which shows that fabric rupture is consistently met in the thin coated group (G-EW), while mixed results are encountered for thick coating (G-ER). Along the same line is crack pattern assessment and again best performance, in terms of crack diffusion and energy dissipation, is reached in the thin coated group. Three-point bending tests suggest that the post-peak behavior of the stress-strain curve is deeply affected by coating thickness and in

19

fact the thin coated group presents a plastic behavior, as opposed to the thick coated group which demonstrates softening. This preliminary study aims at drawing attention on the coating strategy rather than on the coating material, given that only the latter seems to have been investigated in the literature.

6. Declaration of interests

Declarations of interest: none.

Bibliography

[1] RILEM Technical Committee 232-TDT. Test methods and design of textile reinforced concrete. *Materials and Structures*, 49(12):4923–4927, 2016.

[2] ICC AC434. Acceptance criteria for masonry and concrete strengthening using fiber-reinforced cementitious matrix (FRCM) composite systems. *ICC-Evaluation Service, Whittier, CA*, 2013.

[3] F Ascione, L Feo, and F Maceri. An experimental investigation on the bearing failure load of glass fibre/epoxy laminates. *Composites Part B: Engineering*, 40(3):197–205, 2009.

[4] A. Bentur and S. Mindess. *Fibre reinforced cementitious composites*. CRC Press, 2006.

[5] M Butler, S Hempel, and V Mechtcherine. Modelling of ageing effects on crack-bridging behaviour of AR-glass multifilament yarns embedded in cement-based matrix. *Cement and Concrete Research*, 41(4):403–411, 2011.

[6] Z Cohen and A Peled. Effect of nanofillers and production methods to control the interfacial characteristics of glass bundles in textile fabric cement-based composites. *Composites Part A: Applied Science and Manufacturing*, 43(6):962–972, 2012.

[7] J Donnini, V Corinaldesi, and A Nanni. Mechanical properties of FRCM using carbon fabrics with different coating treatments. *Composites Part B: Engineering*, 88:220–228, 2016.

[8] D Dvorkin, A Poursaee, A Peled, and WJ Weiss. Influence of bundle coating on the tensile behavior, bonding, cracking and fluid transport of fabric cement-based composites. *Cement and Concrete Composites*, 42:9–19, 2013.

[9] FO Falope, L Lanzoni, and AM Tarantino. Modified hinged beam test on steel fabric reinforced cementitious matrix (SFRCM). *Composites Part B: Engineering*, 2018. to appear.

[10] SL Gao, E Mäder, and R Plonka. Nanostructured coatings of glass fibers: improvement of alkali resistance and mechanical properties. *Acta Materialia*, 55(3):1043–1052, 2007.

[11] J-K Kim and Y-W Mai. *Engineered interfaces in fiber reinforced composites*. Elsevier, 1998.

[12] V Mechtcherine. Novel cement-based composites for the strengthening and repair of concrete structures. *Construction and Building Materials*, 41:365–373, 2013.

[13] B Mobasher. *Mechanics of fiber and textile reinforced cement composites*. CRC press, 2011.

[14] R Nadiv, A Peled, V Mechtcherine, S Hempel, and C Schroefl. Micro-and nanoparticle mineral coating for enhanced properties of carbon multifilament yarn cement-based composites. *Composites Part B: Engineering*, 111:179–189, 2017.

[15] A Nobili. Durability assessment of impregnated glass fabric reinforced cementitious matrix (GFRCM) composites in the alkaline and saline environments. *Construction and Building Materials*, 105:465–471, 2016.

[16] A Nobili and FO Falope. Impregnated carbon fabric–reinforced cementitious matrix composite for rehabilitation of the Finale Emilia hospital roofs: Case study. *Journal of composites for construction*, 21(4):05017001, 2017.

[17] A Nobili and C Signorini. On the effect of curing time and environmental exposure on impregnated carbon fabric reinforced cementitious matrix (CFRCM) composite with design considerations. *Composites Part B: Engineering*, 112:300–313, 2017.

[18] C Scheffler, SL Gao, R Plonka, E Mäder, S Hempel, M Butler, and V Mechtcherine. Interphase modification of alkali-resistant glass fibres and carbon fibres for textile reinforced concrete I: Fibre properties and durability. *Composites Science and Technology*, 69(3):531–538, 2009.

[19] C Signorini, A Nobili, EI Cedillo Gonzalez, and C Siligardi. Silica coating for interphase bond enhancement of carbon and AR-glass Textile Reinforced Mortar. *Composites Part B: Engineering*, 141:191 – 202, 2018.

[20] C Signorini, A Nobili, and OF Felope. Mechanical performance and crack pattern analysis of aged Carbon Fabric Cementitious Matrix (CFRCM) composites. *Composite Structures*, 2018. 10.1016/j.compstruct.2018.05.052.